

7 3D CFD Analysis of a Diamond Lattice-Based Porous Burner

8
9
10 Pierre-Lou Billerot, Louis Dufresne, Romain Lemaire, Patrice Seers

11
12 TFT laboratory, Department of Mechanical Engineering, École de technologie supérieure, 1100 Notre-
13 Dame Street West, Montréal, Québec, H3C 1K3, Canada

14
15 Corresponding author: Pierre-Lou Billerot pierre-lou.billerot.1@ens.etsmtl.ca
16
17

18 **Highlights**

- 19 • A 3D pore-resolved CFD model of a diamond lattice-based porous burner is proposed
- 20 • The energy recirculation efficiency is maximized under lean-combustion regime
- 21 • Flow pattern is symmetrical until the laminar nonlinear regime is reached
- 22 • Diamond lattice-based porous burner results in a more homogeneous energy release
- 23 • Spatial temperature variations are reduced and more homogeneous

24 **Keywords**

25
26
27
28 3D modeling; combustion; dispersion; pore scale; porous burner, porous media
29
30
31
32
33

34 **Abstract**

35 Innovative 3D metal and ceramic additive printing technologies allow manufacturing porous media with a
36 tailored design pattern, unlike the sponge-like matrices usually used in porous media burners. Based on this
37 technology, this paper aims at modeling, at the pore scale, the flow behavior and combustion features
38 within a structured diamond lattice pattern offering an isotropic and homogeneous porous medium as
39 would be printed using additive manufacturing. A low porosity, 15 pores per inch, porous medium has been
40 tested at equivalence ratios ranging from 0.55 to 0.8. Energy analysis of the proposed 3D model showed
41 that solid radiation losses are negligible compared to solid conduction and convection. The heat transfer
42 analysis reveals that the energy recirculation efficiency reaches a maximum value of 82% at lean-
43 combustion regime. At the pore scale, a symmetrical flow pattern has been observed until a critical
44 Reynolds number of 65 is reached. Based on the flow spatial variations, dispersion has been analyzed and
45 compared with data reported in random structures. Using a lattice structure results in a more homogeneous
46 energy release with less temperature spatial variations. This offers the advantage of decreasing thermal
47 constraints associated with temperature gradients which induce breakage in random structure burners.
48
49
50

51 **1. Introduction**

52 Burners are found in various applications including power plants and households. These devices are also
53 subjected to permanent improvements in order to reach higher efficiency and durability requirements as
54 well as to reduce fuel consumption and pollutant emissions. One approach to reduce pollutant emissions is
55 based on combustion in porous media (CPM). Fundamentally, it consists in burning a reactive mixture
56 within a solid conductive porous matrix. By doing so, the incoming reactants are preheated in the burner by
57 the energy issued from the enthalpy produced by the combustion reactions, such an energy being
58 transported via the solid matrix. Weinberg [1] has been one of the first to introduce the idea of heat
59 recirculation as a means to burn low heat-content fuels. This combustion mode results in a peak
60 temperature somewhat higher than the adiabatic flame temperature and it has therefore been named
61
62
63

1
2
3
4 superadiabatic or excess-enthalpy combustion [2]. Experimental results have identified different CPM
5 benefits such as extended flammability limits [3, 4] as well as high-burning velocity [5, 6]. In addition, the
6 lean-burn capability of CPM leads to relatively low pollutant emissions [7-9], even though the production
7 of CO and NO_x rises as the equivalence ratio and the flame speed increase [8, 10]. A promising upcoming
8 application of CPM is under study [11, 12] and consists in a stabilized ultra-low emission flame generators
9 for gas turbines. In parallel, numerical studies have been widely used to gain insights regarding the
10 phenomena at play within CPM or porous media. The present research reporting on the numerical
11 simulation of CPM, the following literature survey will therefore emphasize on findings related to such a
12 topic.

13
14 As far as the above-mentioned excess of temperature is concerned, it has been found to range from 1% to
15 10% above the adiabatic flame temperature based on the 1D steady laminar modeling work of [13]. Higher
16 excess temperatures ranging from 10% to 20% have been alternatively reported in [14] using a 3D model of
17 a conical burner. Both 1D and 3D models predicted decreasing temperature overshoots as the mixture gets
18 richer, so that the superadiabatic character of the flame vanishes for an equivalence ratio of 0.9 [13, 15].
19 The complexity of the kinetic mechanism used in CPM simulations has also been studied by [16-18], thus
20 showing that dissociation reactions of detailed chemistry lead to lower gas peak temperatures and shallower
21 temperature gradients. This, in turn, results in predictions of flame thickness, temperature profiles, and NO_x
22 emissions in better agreement with experimental data.

23
24 An interesting advantage of CPM relies on the enhanced stability and flammability limits with leaner
25 mixtures [19]. Akbari et al. [20] studied such extended flammability and stability limits using a 1D
26 unsteady laminar model applied to a single-layer cordierite porous matrix having a 0.83 porosity in which
27 the combustion of a methane flame was modeled using a one-step global reaction. Obtained results
28 predicted a lower flammability limit at an equivalence ratio of 0.43 with a firing rate of 50 kW/m², while
29 the lean limit for a free flame of methane is about 0.52 [13]. Barra et al. [21] tried to link the matrix
30 thermophysical properties to the flame-stability limits using a 1D model of a double-layer porous burner.
31 These authors reported that the lower limit is primarily determined by the properties of the upstream
32 section, whereas the upper limit depends on the properties of the downstream section. Moreover, their
33 results showed that a wider flame stability range can be obtained by using low thermal-conductivity
34 materials with a high extinction coefficient in the preheating zone. On the other hand, the reaction zone
35 requires for its part a high conductivity and an optimal pore diameter of 0.152 cm.

36
37 Because of the operating principle of CPM, heat transfers play an important role in the stabilization of the
38 flame at high burning velocities so as to achieve an energy balance in the whole system [3]. Heat transfers
39 have been especially characterized by Barra et al. [22] using a 1D model and by Hashemi et al. [23] using a
40 2D model. Both papers evaluated the relative contribution of each heat transfer mode to the energy
41 transport process and concluded that solid conduction and radiation as well as gas-to-solid and solid-to-gas
42 convection were the main governing heat-transfer modes. Moreover, both studies showed that the heat
43 recirculation decreases at high equivalence ratios and that the burner efficiency also falls with an increasing
44 flame speed ratio defined as the ratio between the interstitial and the laminar flame speed [22].

45
46 The 1D and 2D models discussed above allowed quantifying the macroscopic characteristics of CPM,
47 while 3D calculations have been rarely performed. The main reason for this void in the literature relies on
48 the complexity of the porous-structure geometry, which is usually made of sponge-like foam. Conducted
49 investigations have therefore been often simplified through various approximations including the use of 1D
50 and 2D models likewise volume-averaged Navier-Stokes equations using pressure drop law and effective
51 transport coefficients [24]. Within this framework, heat transfers between the solid and the gaseous phases
52 have been commonly modeled using correlations to estimate the Nusselt number. Indeed, heat transfers in
53 CPM are crucial for the flame stabilization process noting that the design parameters of the matrix are often
54 known unlike its thermal properties. While the simplifications made in the numerical models globally lead
55 to a good general approximation of the burner's behavior, no information on the flow at the pore micro-
56 scale can be predicted, however. Macroscopic models alternatively represent a means to work around the
57 3D mesh-based microstructure representation. Hackert et al. [25] still showed that the flame is highly 2D
58 due to its curvature in porous structures. Moreover and under the commonly used assumptions of 1D and
59 2D simulations, several phenomena such as radial heat losses and hydrodynamic dispersion are neglected
60 thus justifying the need to implement a multidimensional modeling approach [26]. To overcome such
61

1
2
3
4 limitations, 1D models can be modified with an approximation of the root mean square (RMS) values of
5 the gas temperature as done in [27, 28] or by using dispersion coefficients [29]. Although this can allow
6 obtaining a better agreement with experimental data, prior 3D simulations are necessary to compute such
7 values. With this in mind, different studies have addressed the modeling of 3D porous burners using
8 sponge-like structures. For instance, Bedoya et al. [27] conducted a comprehensive study to investigate the
9 influence of the burner geometry, the working pressure and the equivalence ratio on the burning velocity
10 and the flame stabilization. The authors especially compared 1D and 3D calculations with experimental
11 results. The investigated porous-medium geometry was obtained by micro-tomography and consisted of a
12 reticulated sponge sample made of SiSiC with a pore density of 10 PPI (pore per inch) and a porosity of
13 87%. It was observed that the random 3D geometry was responsible for hydrodynamic dispersion, resulting
14 in an increased burning velocity coupled with an enhancement of both thermal and species diffusivities.
15 Indeed, the axial-dispersion coefficient in open-cell foams was found to be two orders of magnitude higher
16 than the molecular diffusivity [30]. The differences observed between 3D and 1D or 2D models were a
17 flatter temperature profile in the former that agrees well with experimentally monitored results, while
18 steeper temperature gradients were observed in 1D model [27] with underestimated flame thickness due to
19 the absence of any cross-section spatial variation in the case of 1D simulations [28].
20

21 That being said, 3D models also contain some simplifications as is the case within the two-layer porous-
22 burner model of Hayashi et al. [31], who used a pressure-drop law in the foam region acting as a
23 combustion chamber. Their results predicted a strong dissipation of the fuel jets from the plate's holes,
24 contributing to stabilizing the flame within the foam. Besides, a statistic-based lattice Boltzmann method
25 has been used by Yamamoto et al. [32] to simulate the flow within a 3D porous foam made of Ni-Cr with
26 the aim of validating such an approach for the simulation of the formation and combustion of soot in a
27 Diesel particulate filter. Microscopic results showed a maximum local velocity eight times higher than the
28 incoming flow due to gas expansion and flow acceleration within narrow passages. This work also
29 highlighted a local peak temperature induced by the inhomogeneous character of the flow.
30

31 Ceramic or metallic foam with a sponge-like structure is the most common medium used for experimenting
32 and simulating flow and combustion in porous burners. The randomness of this type of geometry is
33 responsible for tortuous flow paths and local fluctuations in the stream, as simulated in [27] and observed
34 experimentally in [33] using X-ray computed tomography measurements. Heterogeneous combustion is not
35 desirable because of the related temperature gradients which are responsible for matrix structural stresses
36 induced by differential thermal expansion thus making the matrices brittle [34, 35]. In addition, temporal
37 temperature fluctuations have been reported as being a source of damage for the matrix, as experimented in
38 [36] through a test cycle. The presence of hot or cold spots can, moreover, lead to an increase in NO_x, CO,
39 and unburned hydrocarbon emissions [37]. Contrary to sponge-like foam, porous media with a user-tailored
40 pattern can now be printed thanks to innovative 3D metal and ceramic additive printing technologies. Such
41 an approach allows controlling the shape, orientation, and position of the microstructures [38]. 3D-printed
42 structured media can thus represent an opportunity to reduce flow dispersion by imposing a channeling
43 behavior to the flow through the arrangement of a base pattern in the porous medium. This encourages the
44 evaluation of new geometries with specific lattice patterns for applications in which a fluid-solid contact
45 operates [39]. CPM is part of this framework and very recent studies are exploring this avenue [40-42].
46

47 Within this context, the present work aims at evaluating the efficiency of different geometries of porous
48 media characterized by wide-varied mechanical performances so as to rule on their potential use for
49 combustion applications. More particularly, this paper aims at conducting an energy analysis on a pore-
50 resolved 3D model of a porous burner with a complex isotropic diamond-like structural geometry such as
51 those which could be obtained using advanced additive techniques. Within this framework, a particular
52 attention has been devoted to the analysis of the influence of the inlet conditions on the heat transfers
53 between the gas and the matrix, the burner thermal performances, and the flow behavior. Finally, an
54 overview of the dispersion role has also been investigated based on a comparison with results obtained
55 considering open-cell foams.
56
57
58
59
60
61
62
63
64
65

2. Numerical Setup

2.1. Geometry

As stated in the introduction, the present paper aims at conducting a numerical study of the flow within a porous media having a diamond-lattice structure (see Fig. 1(a)) typical of those obtained using a 3D additive printing technology. The homogeneity of the structure is, thereupon, a noticeable difference with respect to random sponge-like media. A zoom-in on the structure gives a better visualization of the pore scale and outlines the geometry of one pore outlet. This latter can be described as a grid of cylinders angled to each other so as to form a repetitive diamond-like pattern. The diamond-lattice structure is an isotropic geometry and each cylindrical connecting part has an angle of 35.26° with the horizontal plane [43]. The 3D CAD base pattern of such geometry (see Fig. 1(b)) has been used to form the solid porous matrix. As far as the considered fluid region is concerned, it consists of a rectangular box tangent to the matrix from which it has been extracted. Fig. 1(c) illustrates a single element of the fluid domain as an example. For the numerical simulations presented herein, a pore density of 15 PPI and a porosity of 46% have been fixed for the porous medium. The characteristic length known as the pore diameter, D_p , has been chosen as the solid base-pattern height that is equal to 1.7 mm.

The fluid and solid-base repetitive patterns have been combined and stacked to form the representative volume while reproducing the porous medium height. Given the pattern's symmetry, the representation over a single unit (width and length) is sufficient to reproduce the macroscopic porosity of the medium with a volume averaging over the representative domain. The calculation domain of the porous medium consists of a 4.25 cm vertical column of 25 patterns (pores). Eventually, the outer dimensions of the domain (including the fluid phase) are $42.5 \times 1.2 \times 1.2 \text{ mm}^3$.

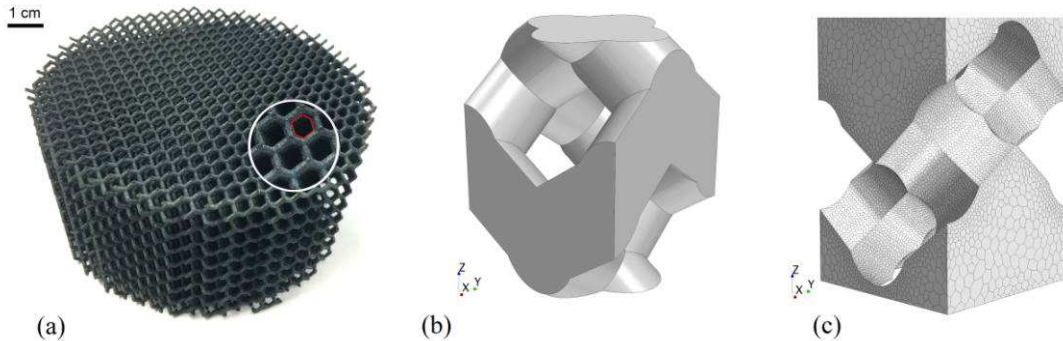


Fig. 1 Porous medium used in this study. (a) 3D printed lattice samples; (b) Solid matrix base pattern; (c) Fluid base pattern with a detailed mesh view

The mesh requirements such as the mesh size and the level of refinement near the walls have been obtained by studying the 3D flow past an isolated circular cylinder (of diameter D) centered in a $40D \times 40D$ extended squared domain. A good representation of the flow has been obtained within an accuracy of 6%-7% on the aerodynamics coefficients (C_D , C_L , C_p) from [44, 45] with 60 nodes equally spaced in the circumferential direction and a maximum cell size in the cylinder's wake corresponding to 5% of the diameter. In the spanwise direction (length of three times the diameter), the mesh resolution close to the cylinder has been kept constant and equal to 5% of the diameter. These mesh characteristics have then been applied to the lattice-shape geometry and the independence of the mesh on the pressure loss through the geometry has been studied based on different mesh configurations (comprising up to more than 3.73 million cells) evaluated with the isolated cylinder. The chosen mesh provided a 1.01% discrepancy on the pressure gradient which has been judged satisfactory. In the end, the computational grid is composed of 1.2 million polyhedral cells in the fluid region and 1.1 million in the solid phase. This mesh configuration results in cell size of $23e-6 \text{ m}$ near the wall and a maximum cell size of $116e-6 \text{ m}$ in the fluid or solid region. The mean cell sizes are respectively $41e-6 \text{ m}$ in the fluid phase and $39e-6 \text{ m}$ in the solid phase.

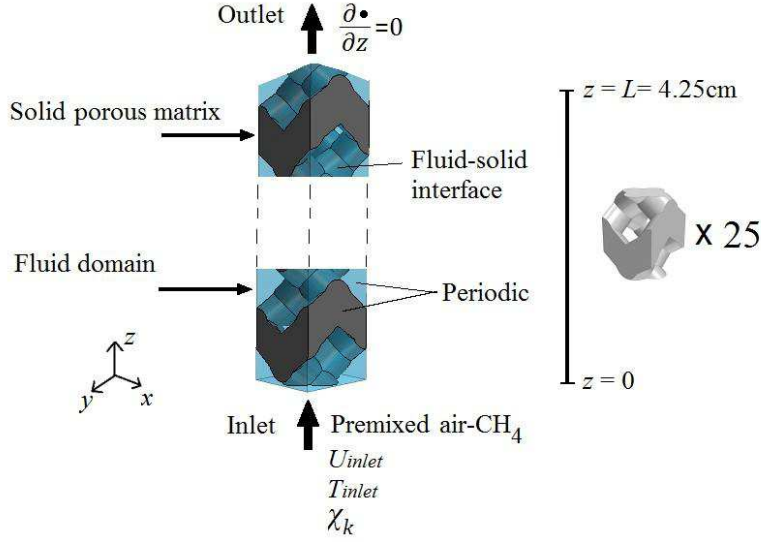


Fig. 2 Computational domain and boundary conditions for CPM modeling

Fig. 2 depicts the computational domain, including the two phases and the boundary conditions. For the different cases run herein, an inlet velocity with a constant profile U_{inlet} has been used as defined in Fig. 3 along with the specified equivalence ratio. The mixture composition has been specified based on the mole fractions χ_k of each component k . The stability limits of the burner have not been precisely determined in this study though the operating conditions simulated were located within the stability domain determined by Liu et al. [46] in a double-layer porous burner. Overall, three cases, denoted A, B and C, have been compared in the present work.

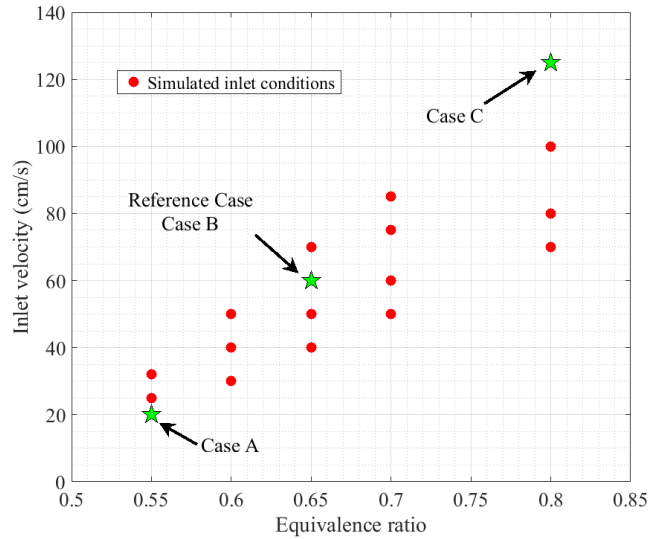


Fig. 3 Tested inlet conditions

In all cases, a fixed inlet temperature of 300 K has been set. At the outlet, a zero normal gradient condition has been implemented for the fluid variables (u , T_f , and χ_k), while a no-slip and non-penetrating condition has been fixed on the wall of the matrix. Following [23, 46], it has been considered that the upper and lower extremities of the solid matrix radiate like a black body towards the environment at ambient temperature. To ensure the solution continuity, a periodic condition has been implemented on the four lateral boundaries of both the fluid and the solid phases.

2.2. Governing Equations

The porous burner has been modeled in 3D. The flow has been treated as being unsteady and presumed as laminar. A two-energy equation model (one for the gas and one for the solid) has been used as the two phases are in non-thermal equilibrium [24]. The gaseous phase interacts with the solid porous matrix via heat convection. It has been assumed that the gas phase behaves as an ideal gas, Dufour and Soret effects being ignored. The continuity equation is depicted by the following relation (Eq. 1):

$$\frac{\partial}{\partial t}[\rho_f] + \nabla \cdot [\rho_f \mathbf{u}] = 0 \quad \#(1)$$

where \mathbf{u} is the velocity vector and ρ_f is the gas density computed by the multi-component ideal gas law (Eq. 2):

$$\rho_f = \frac{p}{RT_f} \frac{1}{\sum_{k=1}^N Y_k / W_k} \quad \#(2)$$

where p denotes the pressure, T_f the gas temperature, R the universal ideal gas constant, while Y_k and W_k stand for the mass fraction and the molar mass of each specie k , respectively.

As far as the momentum equation is concerned, it follows a relation of the type (see Eq. 3):

$$\rho_f \left[\frac{\partial \mathbf{u}}{\partial t} + \mathbf{u} \cdot \nabla \mathbf{u} \right] = \nabla p + \nabla \cdot (\bar{\bar{\tau}}) + \mathbf{f}_b \quad \#(3)$$

where $\bar{\bar{\tau}}$ is the viscous stress tensor and \mathbf{f}_b represents the buoyancy force vector expressed as in Eq. (4):

$$\mathbf{f}_b = (\rho_f - \rho_{ref}) \cdot \mathbf{g} \quad \#(4)$$

Two energy equations have been solved as stated above [47]. Eq. (5) especially represents the conservation of energy in the solid phase:

$$\frac{\partial}{\partial t} [\rho_s C_p T_s] = \nabla \cdot [k_s \nabla T_s] + h_{conv} (T_f - T_s) - \nabla \cdot \dot{\mathbf{q}}_{rad} \quad \#(5)$$

where h_{conv} is the convective heat transfer coefficient while C_p , T_s , k_s , and ρ_s represent the heat capacity, the temperature, the conductivity, and the density, respectively, noting that C_p , k_s , and ρ_s have been considered constant as done in [21]. Besides, the model considers that the porous matrix can emit, absorb, and scatter radiation and acts as a gray homogeneous medium, while gas radiation has not been considered following [13]. The radiative heat flux, denoted $\nabla \cdot \dot{\mathbf{q}}_{rad}$ in Eq. (5), can be written as in Eq. (6) [47]:

$$\nabla \cdot \dot{\mathbf{q}}_{rad} = \int_0^\infty \alpha_\lambda \left[4\pi I_{b\lambda} - \int_{4\pi} I_\lambda(\Omega) d\Omega \right] d\lambda \quad \#(6)$$

where α_λ is the absorption coefficient at the wavelength λ , and $I_{b\lambda}$ is the spectral intensity of a black body evaluated using the Planck's law. The transport of the radiant intensity for a specific wavelength I_λ is governed by the radiative transfer equation (RTE) defined in Eq. (7) [47]:

$$\frac{dI_\lambda}{ds} = \alpha_\lambda I_{b\lambda} - \beta_\lambda I_\lambda + \frac{\delta_\lambda}{4\pi} \int_{4\pi} I_\lambda(\Omega) d\Omega \quad \#(7)$$

where β_λ is the extinction coefficient of the medium obtained by summing the absorption α_λ and scattering δ_λ coefficients. Because the matrix acts as a homogeneous gray medium, such properties are thus

independent of the wavelength. One can finally add that such an equation has been solved using the discrete ordinate method [47].

Table 1 provides the property of the SiSiC porous medium used in the model. Due to the lack of data and correlation to determine the optical properties of ceramic printed structures, the selected optical coefficients have been taken identical to those used in [23] for the SiSiC.

Table 1 Thermophysical and optical properties of the SiSiC porous matrix [23, 48]

Property	Value	Unit
Porosity Φ	0.46	-
Density ρ_s	2900	kg/m ³
Specific heat Cp_s	1100	J/kg-K
Thermal conductivity k_s	18	W/m-K
Absorption coefficient α	28	1/m
Scattering coefficient δ	66	1/m
Emmissivity ϵ	0.9	-

Concerning the conservation of energy in the fluid phase, it is represented by Eq. (8) noting that the two energy equations are coupled by h_{conv} with a conjugate heat transfer boundary condition at the fluid-solid interface.

$$\begin{aligned} \frac{\partial}{\partial t} [\rho_f Cp_f T_f] + \nabla \cdot [\rho_f Cp_f T_f \mathbf{u}] + \nabla \cdot \left[\sum (J_k Cp_f T_f) \right] + Q_{ch} \quad \#(8) \\ = -h_{conv}(T_f - T_s) + \nabla \cdot [(k_f + \rho_f Cp_f D_d^d) \nabla T_f] \end{aligned}$$

The D_d^d term within Eq. (8) represents the thermal diffusivity due to dispersion. The rate of heat release from the chemical reactions defined as $Q_{ch} = \sum_k (\dot{\omega}_k h_k W_k)$ has been computed based on $\dot{\omega}_k$, which is the production/destruction rate of each specie k . The gas specific heat Cp_f has been calculated using the mass-weighted mixture method, while the thermal conductivity follows the Mathur-Saxena averaging method based on the mole fractions of the different species [47].

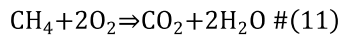
Lastly, an equation for species conservation has been solved (Eq. 9):

$$\frac{\partial}{\partial t} [\rho_f Y_k] + \nabla \cdot [\rho_f Y_k \mathbf{u}] = \nabla \cdot [\rho_f D_{k,m} \nabla Y_k] + \dot{\omega}_k W_k \quad \#(9)$$

The diffusive flux has been evaluated based on the Fick's law using the kinetic theory for the calculation of the molecular diffusivity of the specie k in the mixture. Concerning the binary diffusion coefficient between species k and j , D_{kj} , it has been calculated following Eq. (10):

$$D_{k,m} = \frac{1 - \chi_k}{\sum_{j=1, j \neq k}^N \frac{\chi_j}{D_{kj}}} \quad \#(10)$$

The combustion has been modeled with an irreversible one-step global reaction to reduce the computational cost. The unidirectional air-methane combustion reaction can be summarized as depicted within Eq. (11):



This kinetic is in fact dictated by reaction coefficients and governed by an Arrhenius law allowing $\dot{\omega}_k$ to be estimated based on Eq. (12):

$$\dot{\omega}_k = \frac{d[X_k]}{dt} = (v_k' - v_k'') \left[AT^n \exp\left(-\frac{E_a}{RT}\right) \right]_k \prod_{j=1}^N [X_k]^{v_j} \quad \#(12)$$

where the Arrhenius coefficients have been taken from [49], the pre-exponential factor, A , has been set to $2.119^E 11 \text{ cm}^{1.5} \cdot \text{mol}^{-0.5} \cdot \text{s}^{-1}$; the activation energy E_a has been considered as being equal to 48.4 kcal/mol, the temperature exponent, n , has been set to zero while the reaction orders for each reactant have been defined as follows: $\nu'_{\text{CH}_4} = 0.2$ and $\nu'_{\text{O}_2} = 1.3$.

The above equations have been solved with the commercial CFD software STAR-CCM+ using the finite volume method. The SIMPLE (Semi-Implicit Method for Pressure-Linked Equation) algorithm has been selected to solve the coupling between the pressure and the velocity in the momentum equation. A second-order implicit formulation has been used for the temporal discretization with a time step of 10^{-5} s. A second-order upwind scheme has been implemented for the spatial discretization while a second-order scheme has been used for the discretization of the unsteady and convection terms in the transport equation. For all the cases considered herein, a convergence criterion of 10^{-6} has been fixed.

3. Model Validation

3.1. Isothermal Flow Simulation

A nonreactive gas flowing through the porous medium described in section 2.1 has been simulated as an intermediate validation step. The inlet velocity has been varied from 1 to 150 cm/s, thus corresponding to Reynolds numbers (based on the pore diameter (Eq. 13)) ranging from 1 to 115:

$$Re_p = \frac{\rho_f u_D D_p}{\mu} \quad \#(13)$$

where μ is the gas dynamic viscosity and u_D is the superficial velocity. Three flow regimes have been identified, as illustrated in Fig. 4(a), by analyzing the nondimensional macroscopic pressure gradient $\frac{\partial p}{\partial z} \left(\frac{D_p^2}{\mu u_D} \right)$ through the column as a function of Re_p . Graphically, a flow regime transition can be identified by a change in the slope of the reduced pressure drop [50]. Based on Fig. 4, one can thus differentiate between the Darcy regime associated with low Reynolds numbers ($Re_p < 6$) in which the viscous forces dominate, the inertial Forchheimer regime ($6 \leq Re_p \leq 65 \pm 5$), and the nonlinear laminar regime for higher Reynolds numbers at which the inertial force is predominant as the velocity gradually increases. In these different regimes, the flow is laminar and steady without temporal fluctuations. Note that the Forchheimer regime is also a nonlinear regime although the post-Forchheimer regime can be qualified as a strong inertial regime while being turbulence precursory. The non-reacting model has been compared to the Darcy-Forchheimer pressure drop law using the correlations proposed by Ergun [51] and Fand et al. [52] based on the porosity and pore diameter as shown in Fig. 4(b). The numerical results are quite consistent with the correlation from [52] for most of the inlet velocities considered in the Forchheimer regime, although it falls for the highest velocities because the pressure drop law is not appropriate for flows characterized by high Reynolds numbers.

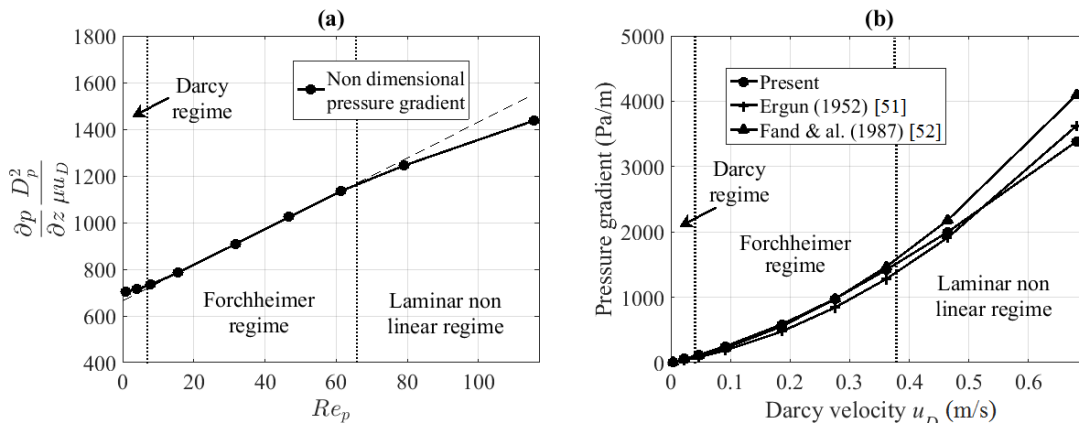


Fig. 4 Macroscopic pressure gradient.
(a) Identification of the flow regimes; (b) Pressure drop law verification

3.2. Combustion Baseline Simulation – Temperature Profiles

A baseline simulation has been used as a reference case to validate the approach implemented within the present work. In this case, the inlet conditions were representative of CPM and correspond to an air–methane mixture with an equivalence ratio of 0.65 with an inlet velocity of 0.6 m/s (Case B in Fig. 3) as previously used in [21, 46]. The gas temperature, the solid-phase temperature and the energy-released profiles are plotted in Fig. 5 along the axial direction of the burner. The reported results are mass flow averaged values on a cross-sectional surface along the domain. The resolution in the axial direction is 4 planes/mm. Since the studied flame is laminar and premixed, its structure (i.e. the temperature profile) can be divided into different regions as in [21, 53]. Barra et al. [21] suggested that the beginning of the preheating region can be defined by a 1% gas temperature increase from its initial temperature. Given the fast initial increase of the gas temperature observed in Fig. 5, the preheating region is considered to begin after the inlet boundary. This quick rise in the gas temperature is due to the high temperature of the matrix at the inlet (621 K) because of the material’s high thermal conductivity. High thermal conductivity indeed enhances heat transfers and hence leads to an increase of the matrix temperature [46]. Moreover, the tortuous 3D path of the flow induces spatial variations of the temperature in the fluid that contributes to increasing heat transfers due to an enhancement in both heat and mass transport phenomena [27]. The preheating zone shows that the temperature of the matrix is higher than the unburned gas temperature while the gas- and solid-phase temperature profiles intersect between 1.7 and 1.9 cm from the inlet. This location can be considered as the end of the preheating zone (inset area) where the reaction zone begins with an associated bulk energy release and a gas temperature higher than the solid ones. The peak of energy released indicates the position where the flame stabilizes, namely 2.12 cm downstream of the inlet in this case. The reaction zone ends where the extrapolated heat release curve intercepts the abscissa axis. The two phases have approximately the same temperature in the post-flame zone and can be considered in thermal equilibrium.

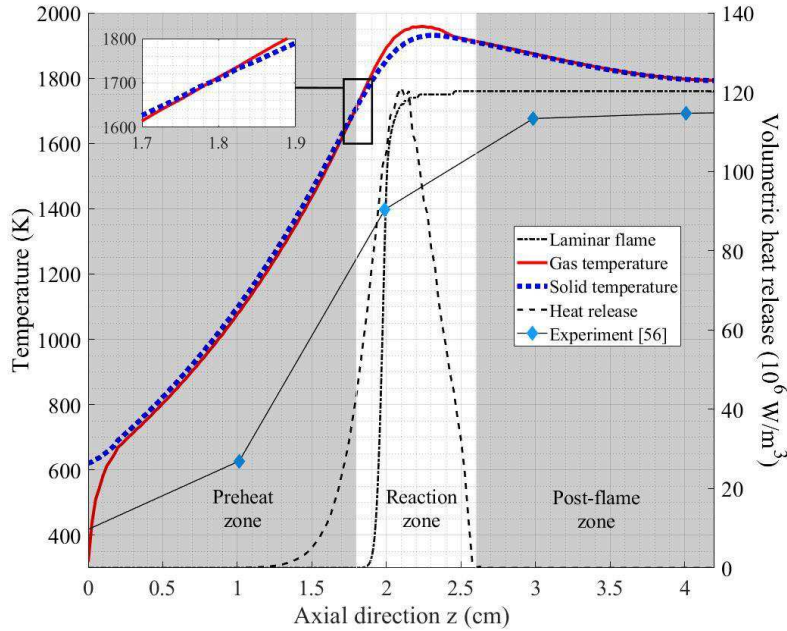


Fig. 5 Profiles of heat release together with solid and gas temperatures for the baseline simulation

The predicted temperature profiles are more flattened and stretched than the laminar flame profile obtained with Chemkin using the Gri-mech 3.0 chemical kinetic [54], as illustrated in Fig. 5. Based on these results, the flame thickness has been computed based on the maximum temperature gradient or thermal thickness [55] following Eq. (14):

$$\delta_L = \frac{T_{f,max} - T_{f,z=0}}{\max\left(\frac{dT_f}{dz}\right)} \quad \#(14)$$

For the CPM modeled herein, the flame thickness is equal to 17 mm, which is about 9 times the thickness of the free laminar flame (2 mm). Such a trend is quite consistent with the experimental results of [27] which exhibit an increase of the flame thickness by a factor of 10 when using a sponge-based porous burner. The increase of the flame thickness observed in CPM can in fact be linked to the higher effective diffusivity coefficient, which increases the thermal diffusivity. In CPM, however, the thermal diffusivity is a function of axial dispersion and heat recirculation. As reported by Bedoya et al. [27], the flow within CPM indicates dispersion coefficients higher than the molecular diffusivity. Thus, the better heat transport properties of the gas due to dispersion lead to a broadened reaction zone and thus increase the flame thickness, as depicted in Fig. 5. A comparison with the experimental results of [56] obtained with a 10 PPI SiSiC open-cell foam at an equivalence ratio of 0.625 is proposed in Fig. 5. Such results exhibit a stretched flame (one of the main characteristics of CPM) which is also observed in the modeling results, thus confirming the approach considered herein. In the reaction zone, the gas profile reaches a peak temperature of 1958 K, which is 198 K above the adiabatic-flame temperature. This temperature overshoot of 11% corresponds to a superadiabatic combustion due to the presence of the solid matrix that preheats the reactants (as commented in the next section) and increases the reaction enthalpy. Similar temperature overshoots have also been reported in the literature such as in [21] where a peak temperature of 50K above the adiabatic flame temperature has been observed using the GRI 1.2 kinetic (177 reactions).

4. Macroscopic Results

4.1. Heat Transfer and Recirculation

The local temperature difference between the fluid and the solid phases induces heat transfers from one phase to another. This temperature gap is apparent in Fig. 5 (the difference $T_s - T_f$ in the preheating zone after the inlet boundary being of about 20 K). The largest deviation is observed at the inlet of the burner because the incoming mixture is at ambient temperature while the solid matrix has reached a higher temperature (~600 K) due to heat conduction. In the preheating zone, there is a small temperature difference between the unburnt mixture and the solid medium, suggesting an effective reactant preheating. Finally, a temperature difference of approximately 40 K can be observed in the region of enthalpy generation of the reaction zone.

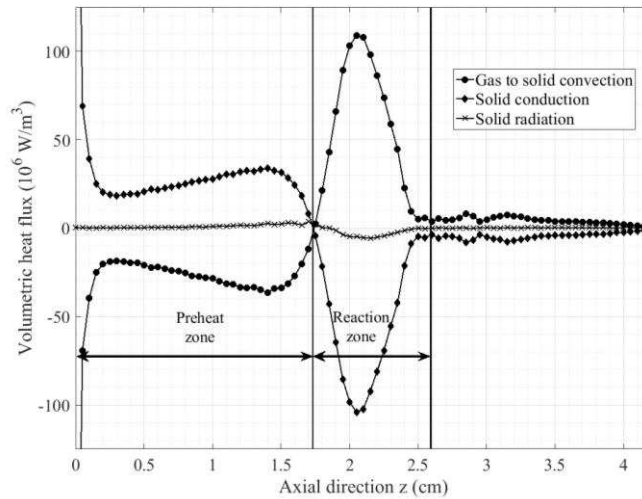


Fig. 6 Energy budget on the solid interface for the baseline simulation

Fig. 6 depicts the energy balance on the solid interface in a steady-state regime. The sign convention implies that a flux leaving the surface is positive. In the reaction zone, the bulk of heat is released by the chemical reaction, so that the gas temperature is higher than the matrix temperature. The convection heat

flux from gas to solid is therefore positive. This energy is transported within the solid matrix from the reaction zone to the preheating zone by both solid conduction and radiation. The flux is reversed in the preheating zone where the solid temperature is higher than the gas one thus leading the matrix to heat the unburned gases by convection. The reactant preheating is so due to the combination of convection, solid conduction and radiation. The amount of convective heat recirculated in the preheating zone between the gas and solid phases is the sum of the solid conductive and radiative heat recirculation from the reaction zone into the preheating one [23]. Therefore, convection is balanced by radiation and conduction, as can be verified in Fig. 6. Moreover, Fig. 6 shows that solid conduction plays a dominant role in the recirculation process relative to solid radiation for the considered case. Thus, radiation can be omitted as in [27] but only in 3D models. Indeed, results obtained with 1D [15, 22] and 2D [23, 57] models have shown that radiation is crucial since, in these latter, the heat gained by the solid in the reaction zone is mostly balanced by radiation. Moreover, the energy-balance analysis of a 2D model in [58] with a combined porous-free flame burner showed that the contributions of radiation and conduction were of the same order of magnitude.

4.2. Porous-Burner Efficiency

The influence of the inlet velocity and equivalence ratio on the heat recirculation process has been studied over a range of operating conditions representative of CPM, as shown in Fig. 3. The equivalence ratio and the inlet velocity have been varied from 0.55 to 0.8 and 20 cm/s to 125 cm/s, respectively. The burner efficiency for each operating point has been calculated by evaluating the relative contribution of each individual transfer mode to the heat recirculation process as a function of the gas speed ratio (*GSR*) defined by Eq. (15) [22]:

$$GSR = \frac{\text{Superficial velocity}}{\text{Laminar flame speed}} = \Phi \frac{\langle u_z \rangle}{S_L} \quad \#(15)$$

Both conduction and radiation in the solid participate to the recirculation process, so that their relative contributions to the heat recirculation mechanism are defined based on Eqns. (16) and (17), respectively:

$$\begin{aligned} &\text{Preheating conduction efficiency} = \\ &\frac{\text{Solid conduction into the preheating zone}}{\text{Chemical thermal power}} = \frac{\iint_{\text{Reaction zone}} |\dot{q}_{cond}| dS - \iint_{\text{Post-flame zone}} |\dot{q}_{cond}| dS}{\iiint_{V_f} Q_{ch} dV} \quad \#(16) \end{aligned}$$

$$\begin{aligned} &\text{Preheating radiation efficiency} = \\ &\frac{\text{Solid radiation into the preheating zone}}{\text{Chemical thermal power}} = \frac{\iint_{\text{Reaction zone}} |\dot{q}_{rad}| dS - \iint_{\text{Post-flame zone}} |\dot{q}_{rad}| dS}{\iiint_{V_f} Q_{ch} dV} \quad \#(17) \end{aligned}$$

Finally, the total amount of heat recirculating in the burner by the convective exchange from the matrix to the gas in the preheating zone is defined by Eq. (18):

$$\begin{aligned} &\text{Convective heat recirculation efficiency} = \\ &\frac{\text{Solid - to - gas convection in the preheating zone}}{\text{Chemical thermal power}} = \frac{\iint_{\text{Preheating zone}} |\dot{q}_{conv}| dS}{\iiint_{V_f} Q_{ch} dV} \quad \#(18) \end{aligned}$$

Since convection is balanced by the conduction and radiation terms, Eq. (18) is the sum of Eq. (16) and Eq. (17), as mentioned in section 4.1. The fraction of heat transported by conduction and radiation from the reaction zone into the post-flame zone throughout the solid matrix does not participate to the recirculation process or reactant preheating. Thus, this corresponding heat flux has been removed in Eqns. (16) and (17) from the flux transferred to the matrix into the reaction zone.

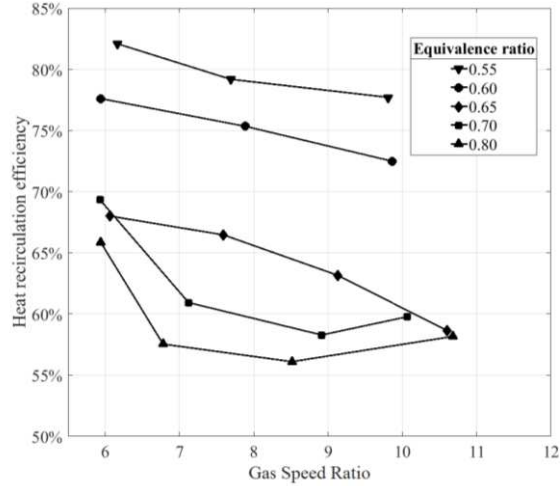


Fig. 7 Heat recirculation efficiency as a function of the GSR

The evolution of the heat recirculation efficiency is shown in Fig. 7 as a function of the GSR. As can be seen, higher values of the heat recirculation efficiency are obtained at low equivalence ratios due to lower gas inlet velocities. Similarly, at an iso-equivalence ratio, the efficiency also increases as the gas velocity decreases. Indeed, as the inlet velocity is reduced for an identical equivalence ratio, or for decreasing equivalence ratio at constant GSR, the residence time of the incoming gas in the preheating zone increases [14]. The preheating temperature is then higher due to an enhanced heat transfer between the solid and the gas. The heat recirculation efficiency ranges from 77% to 82% at an equivalence ratio of 0.55 and from 58% to 66% for an equivalence ratio of 0.8. While evidencing the same trend, these values are considerably higher than the efficiency found by Barra et al. [22], Hashemi et al. [23], Hashemi et al. [58] as well as higher than the efficiency obtained with 1D and 2D models. This difference is due to the low porosity of the matrix modeled herein (0.46 versus ~ 0.77 - 0.87) reminding that a low porosity favors heat diffusion in the solid and increases heat recirculation as reported by [59].

Fig. 7 also illustrates a reversal in the heat recirculation efficiency for the highest GSR values and for the two highest equivalence ratios tested herein, namely 0.7 and 0.8. This change in behavior might be associated with a modification of the flow, from the Forchheimer to the laminar nonlinear regime. Indeed, the Re_p corresponding to the operating conditions where a deviation is noticed in Fig. 7 is close to the critical value of 65 ± 5 reported in section 3.1. Hence, the laminar Forchheimer flow turns progressively into the nonlinear laminar regime, which enhances both mass and heat transport properties, resulting in a more efficient heat transfer. Nonetheless, the recirculation efficiency in the nonlinear laminar regime remains below the one reached for the lowest equivalence ratios.

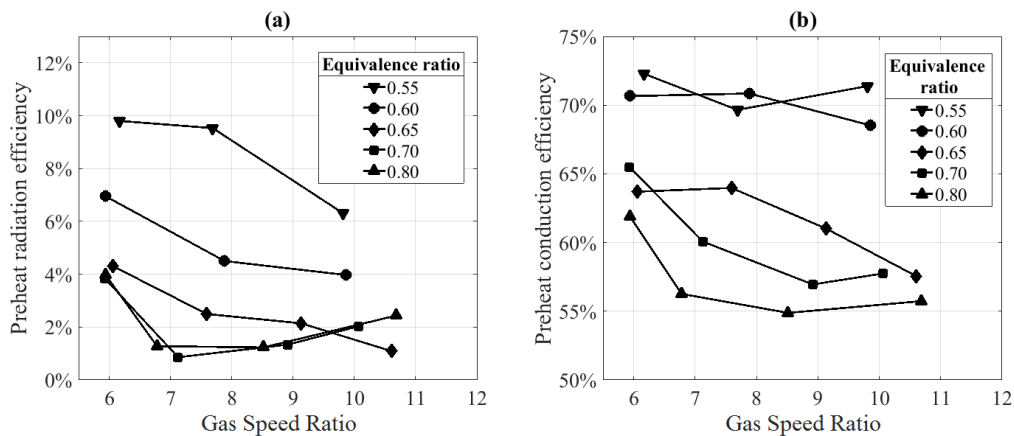


Fig. 8 Preheating efficiency as a function of the GSR. (a) Solid radiation; (b) Solid conduction

The contribution of radiation in terms of recirculation efficiency (illustrated in Fig. 8(a)) follows a similar trend with values in good agreement with those found in the above-mentioned studies, thus confirming that the contribution of radiation can be neglected at equivalence ratios higher than 0.6. Since the heat recirculation efficiency is a function of both the radiative and conductive preheating efficiency, the discrepancy with [22, 23] can be attributed to at least two factors. First, the higher contribution of conduction herein (see Fig. 8(b)) can be linked to the higher thermal conductivity of the material, which is 90 times higher than the value used in [22]. Secondly, the dispersion in the flow due to its tortuous path is also an important feature that can enhance the heat transport to the gas phase [27], while the tortuosity and the 3D spatial variations in the flow are, quite logically, not effectively represented in 1D and 2D models.

5. Microscopic Observations

Subsequent to the above energy balance study, the analysis now turns to the pore-scale level in order to compare the flow and combustion features within a structured geometry with the behavior reported in the literature for foams [27, 32, 60]. First, the scalar velocity fields and streamlines along the temperature distribution have been analyzed. The area of interest is located in the reaction zone where the peak temperature is reached, and the results are represented over a length of 10 mm. Three cases are presented to illustrate the different inlet conditions introduced in Fig. 3 and summarized in Table 2. Cases A and C correspond to extremums studied with different flow regimes.

Table 2 Inlet conditions for the different cases compared

Case	Inlet Velocity U_{inlet} (m/s)	Equivalence Ratio φ	Comment
A	0.20	0.55	Lowest inlet condition tested
B	0.65	0.65	Reference case
C	1.25	0.80	Highest inlet condition tested

5.1. Velocity Fields

Fig. 9 depicts the scalar fields of the velocity magnitude on a longitudinal cross-sectional plane of the column at different heights in the porous column. In the vicinity of the reaction zone, the local velocity magnitude reaches high values due to the high gas temperature (and its associated low gas density), which is a function of the energy released and thus of the equivalence ratio. The matrix microstructure has a narrow opening leading the flow to accelerate and decelerate near the solid walls. The maximum nondimensional velocities u/U_{inlet} reached by the gas are, respectively, 12.1 in case A, 14.6 in the reference case, and up to 18.2 in case C.

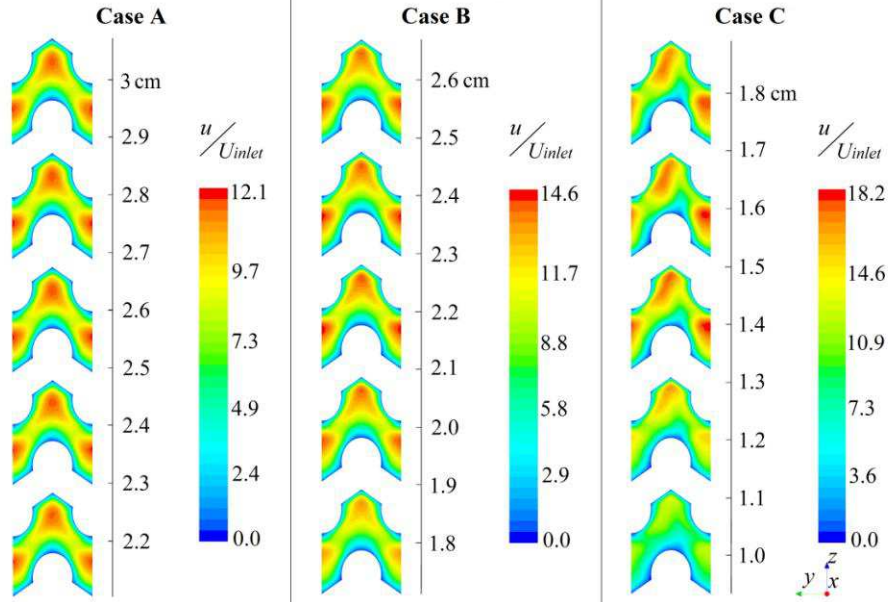


Fig. 9 Microscopic velocity fields on longitudinal planes centered on the reaction zone

The values of the volume-averaged pore Reynolds numbers (Re_p) are of 13 and 39 in cases A and B, respectively, thus corresponding to the Forchheimer regime. In such a configuration, the flow is symmetrical and steady regardless of the observation plane. Similarly to the flow through a staggered arrangement of circular cylinders, it reaches the upstream section of the cylindrical parts (stagnation point), accelerates within the pore, and then reattaches downstream of the cylindrical parts without recirculation. In contrast, case C has a Re_p of 85 that can be identified as corresponding to the nonlinear laminar regime. In this regime, the flow deviates from its axial path downstream of the cylindrical parts. The flow symmetry is thus broken, but the flow pattern repeats itself throughout the column without oscillations. To get a better representation of the phenomena at play between the Forchheimer and the nonlinear laminar regimes, streamlines of the flow for cases B and C are analyzed below. Corresponding results are shown in Fig. 10 where the solid matrix is also illustrated with its temperature fields. Two adjacent columns are presented due to the periodic condition on the lateral faces. In the reference case (Fig. 10, left), the streamlines are ordered with a helical profile. A focus on one streamline suggests that the fluid is flowing in a quarter of the column without passing through its symmetry planes or crossing with another neighbor streamline. This preferential stream refers to a channeling behavior with an angular symmetry of the flow. In contrast, flow confinement is not observed in the nonlinear laminar regime of case C (Fig. 10, right) as streamlines leaving the domain and/or crossing other streamlines are seen. Due to the periodicity of the solution, a streamline leaving the domain through one face implies an incoming streamline on the opposite face. Inertial forces in the nonlinear laminar regime play an important role and are responsible for this behavior.

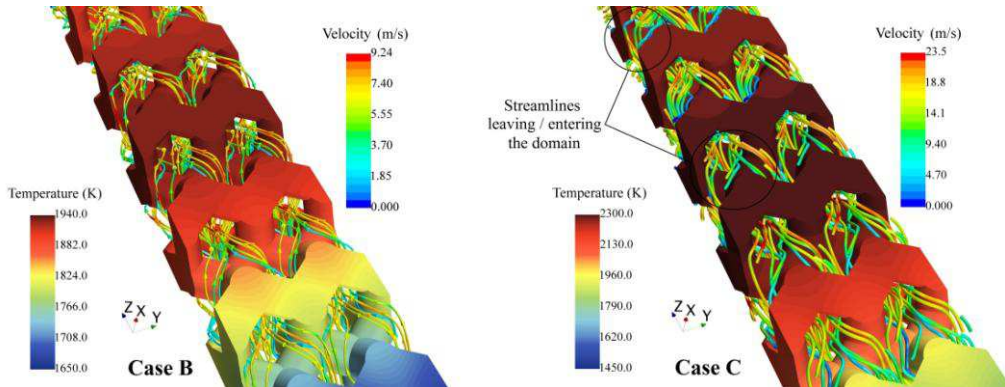


Fig. 10 Streamlines through the matrix. Left: Reference case B; Right: Case C

5.2. Dispersion and Mixing Quantification

Based on the above observations, it appears that a change in the flow regime impacts the components of the velocity vector u_j . This consequence has been further investigated with an analysis of the spatial fluctuations of the velocity components so as to quantify the mixing process. These fluctuations have been calculated as the RMS value of each component along the longitudinal direction using Eq. (19) as in [27] over the considered domain discretized into 170 cross-sectional planes (4 planes/mm).

$$u_{j,rms} = \sqrt{\frac{1}{n-1} \sum_{i=1}^{n-1} (u_{j,i} - \langle u_j \rangle)^2} \quad \#(19)$$

To facilitate comparison between the studied cases, the RMS value of each velocity direction has been divided by the local bulk velocity $\langle \mathbf{u} \rangle$ so as to obtain the nondimensional values presented in Fig. 11.

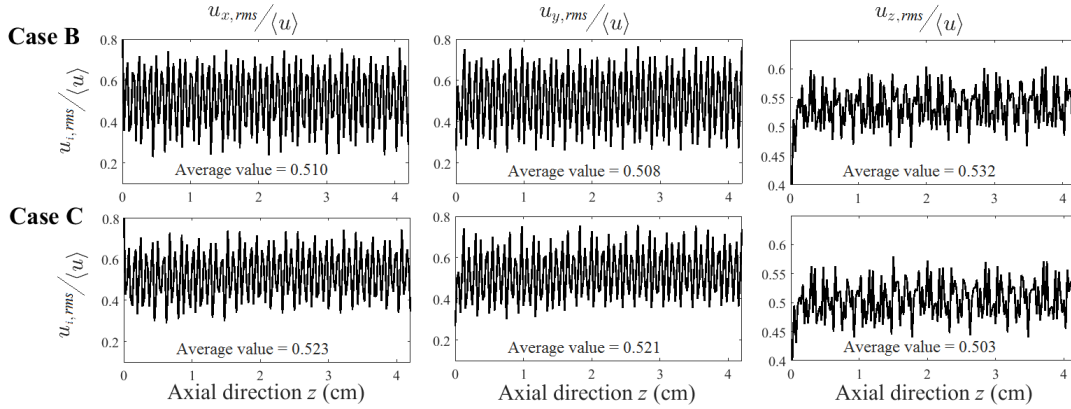


Fig. 11 Spatial fluctuations of the velocity components for cases B and C

Since results obtained for cases A and B are very similar, only data for cases B and C have been presented in Fig. 11. Besides, Table 3 presents the adimensional mean spatial fluctuations of each velocity component for the three considered cases in order to illustrate the similarity between cases A and B, which are both in the Forchheimer regime. For the three cases, Table 3 shows that the non-dimensional mean spatial velocity is between 50% and 54%, suggesting a comparable dispersion in all directions. In open-cell foams with higher porosity (0.74 to 0.87) and larger pore density (10 to 45 pores per inch), [30] reported adimensional axial velocity fluctuations between 47% and 66%. In contrast to the data summarized in Table 3, the results of [30] present a domination of axial-velocity fluctuations. The trends highlighted herein thus suggest that the axial velocity fluctuation ($u_{z,rms}$) is slightly dominant while its weigh decreases as the Reynolds number increases. As the flow reaches the characteristics associated with the nonlinear laminar regime (case C), deviations in the flow occur, as observed based on the streamlines. This behavior translates into higher mean spatial fluctuations of the transverse velocity components with respect to the longitudinal velocity (see Table 3).

Table 3 Mean spatial fluctuations of the velocity components

Case	Regime	$\frac{u_{x,rms}}{\langle u \rangle}$	$\frac{u_{y,rms}}{\langle u \rangle}$	$\frac{u_{z,rms}}{\langle u \rangle}$
A	Forchheimer	0.510	0.508	0.544
B	Forchheimer	0.510	0.508	0.532
C	Nonlinear laminar	0.523	0.521	0.503

It can be concluded that the higher inertial forces of case C with respect to cases A and B results in a larger flow deviation in the transverse directions (x and y), as observed in Fig. 9, which thus influences the

dispersion in the fluid phase. Dispersion in porous media is the combination of convective diffusion (or mechanical dispersion) and molecular diffusion phenomena [61] (the overall process being referred as hydrodynamic dispersion). The convective diffusion combined with the presence of pores and matrix strut cause the flow to move laterally, resulting in spatial variations in velocity, both in magnitude and direction, and thus a shift from axial momentum to radial or transverse momentum [62, 63].

As Parthasarathy et al. [30] used the axial dispersion as a mixing indicator within the flow, it has also been used herein to confirm that the dispersion is similar in all three directions. This provides a comparison between the dispersion in structured porous media versus the one reported in the literature for open-cell foams or packed beds with the longitudinal dispersion coefficient (D_L). As D_L is typically determined from isothermal flow, isothermal simulations of air with average Re_p equivalent to cases A, B, and C (denoted A', B', and C', respectively) have been conducted. Following a procedure similar to the one used in [29, 30], a method of moments based on the time history of the passive tracer concentration within the medium has been used. The description of the method of moments is provided in the Supplementary Materials. The values of the dispersion coefficients and dispersion ratio D_L/D_m have been calculated for cases A', B' and C' as reported in Table 4. Obtained results indicate that, as the velocity increases, the dispersion due to the convective diffusion is more prominent with respect to the molecular diffusion assumed constant in the simulation.

Table 4 Dispersion study results

Case	Re_p	$D_L (\times 10^{-5})$ (m ² /s)	D_L/D_m	Pe_m
A'	12	0.97	0.746	18.5
B'	38	2.89	2.22	59.5
C'	89	8.60	6.62	150.5

The Peclet number Pe_m based on the molecular diffusion coefficient is commonly used as a nondimensional ratio between the convective and the molecular diffusion. It is expressed as proposed in Eq. (20):

$$Pe_m = \frac{\langle u \rangle D_p}{D_m} \quad \#(20)$$

where D_p is the pore diameter (i.e., the characteristic length scale). The dispersion results using the above procedure are compared in Fig. 12 to the data available in the literature for gas dispersion in packed beds and in open-cell foams [30, 64]. It should be noted that the linear relationship between the dispersion ratio and the Peclet number reported in the literature has also been found in this study and that the slope has also been well predicted. The values of the dispersion ratio are smaller than those for open-cell foams or packed beds, however, thus suggesting that the matrix's structured geometry induces less dispersion than conventional foams and packed beds. Although the overall dispersion is reduced, the relative dispersion rise observed in the cases tested within this work tends to enhance transverse mixing in the fluid.

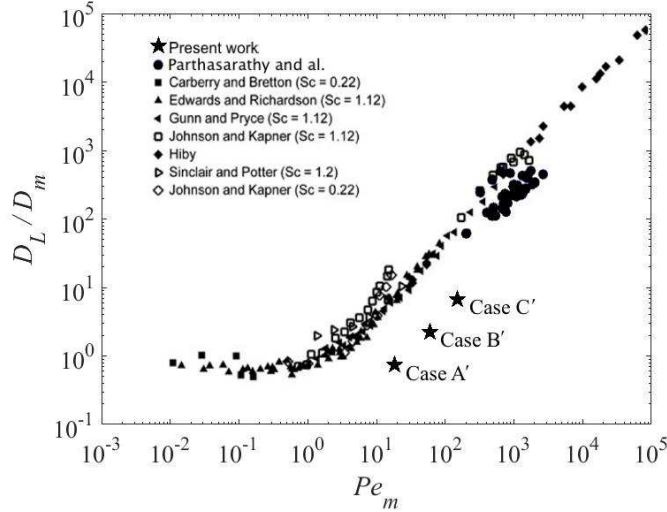


Fig. 12 Comparison of the dispersion ratio of the flow in a diamond-lattice structure, packed beds and open-cell foams (adapted from [30])

5.3. Temperature Distribution

Fig. 13 presents the temperature field and its longitudinal distribution for cases A, B, and C. The graphs are centered on the peak temperature in the reaction zone over a length of 10 mm. The temperature contours are plotted for the fluid and solid phases. At a given ordinate z , the gas is hotter in the middle of the interstice because the flame cannot propagate on the wall. Indeed, the no-slip condition on the wall slows down the reaction. As the mixture gets leaner while its inlet velocity becomes lower (from case C to A), the locations of the highest temperature spots are spread over a longer distance. As mentioned in section 3.2, the reaction zone begins where the gas and the solid temperature profiles are equal. This location is not visible for case A. For cases B and C, this location moves towards the peak temperature location as the equivalence ratio and the inlet velocity increase. As a consequence, the reaction zone is narrower with values of 13.2 mm, 8 mm, and 2.9 mm for cases A, B, and C, respectively.

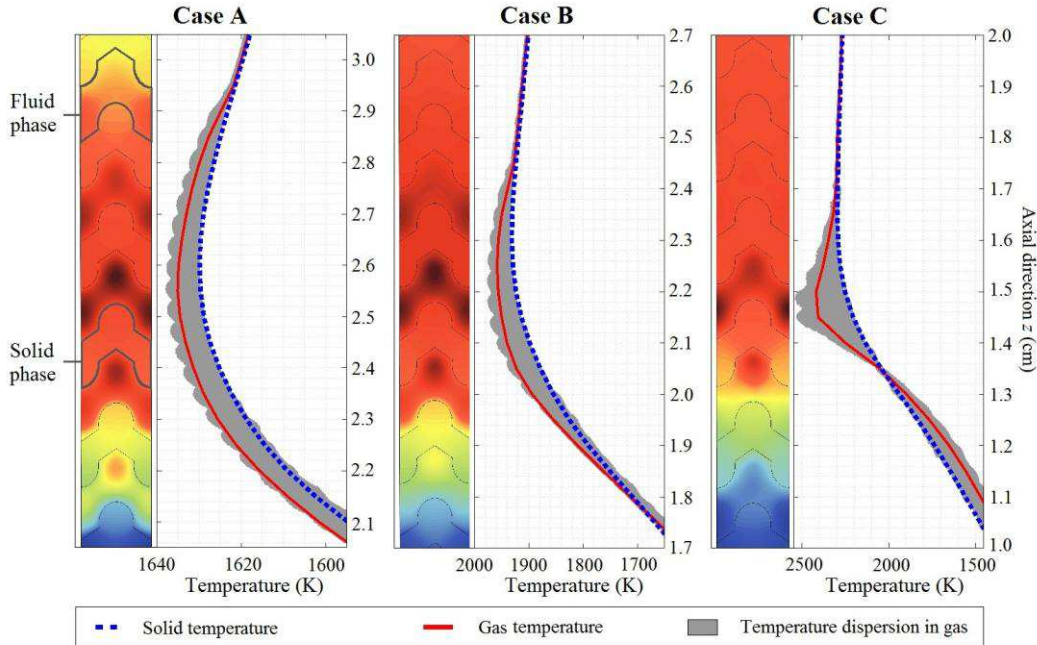


Fig. 13 Longitudinal distribution and scalar fields of the temperature

The spatial variations of the temperature are more pronounced as the inlet velocity and the equivalence ratio increase. This is due to the dispersion in the fluid, which increases, as mentioned above. These spatial variations of the gas temperature are depicted in Fig. 14 using the RMS of the temperature, $T_{f,rms}$ expressed as in Eq. (21):

$$T_{f,rms} = \sqrt{\frac{1}{n-1} \sum_{i=1}^{n-1} (T_{f,i} - \langle T_f \rangle)^2} \quad \#(21)$$

The longitudinal direction has been discretized into 170 cross-sectional planes (4 planes/mm) to calculate the RMS values. The temperature dispersion in the gas in case A is relatively homogeneous and low in value. The variations are more pronounced for cases B and C where the dispersion increases and suddenly drops in the preheating zone. At this particular location, the spatial variations are low because it corresponds to the entry of the reaction zone where the solid and gas temperature profiles are equal. Then, the dispersion increases in the reaction zone to a peak value of 3 K for case A, 18 K for the reference case, and 93 K for case C. In the post-flame zone, the dispersion reaches the value of zero because the fluid and the solid phases can be considered as in thermal equilibrium. As observed in Fig. 14, the RMS of the gas temperature profile follows a trend similar to the gas temperature gradient profile (also shown therein). This similitude has been used to reproduce the spatial variations of the gas temperature using the temperature RMS to improve a 1D model in [27].

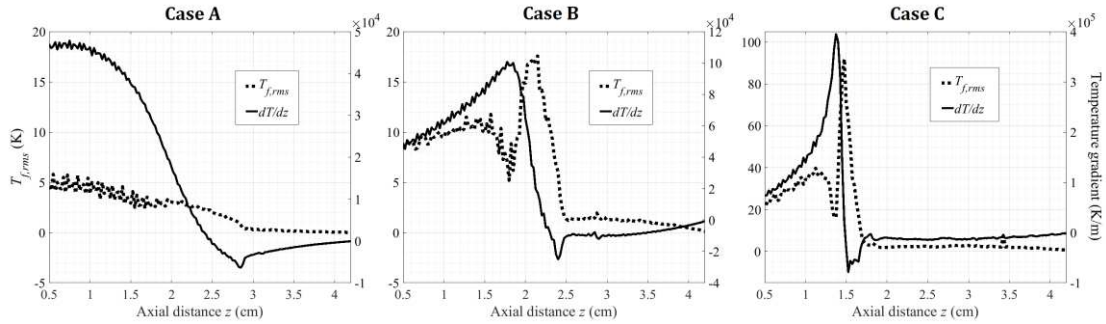


Fig. 14 Temperature gradient and RMS distribution of gas temperature

Fig. 14 clearly shows that the spatial temperature fluctuations decrease under lean combustion regimes due to the associated low inlet velocity for such mixtures. The temperature fields recorded by [27, 32, 33] in randomly structured porous media showed high combustion inhomogeneity in the reaction zone. Herein, no local hot or cold spots with a high temperature gradient are visible in the gas. Consequently, the results obtained within this work suggest that the use of a structured and isotropic matrix reduces combustion inhomogeneity as well as local temperature gradients. This might be beneficial for the matrix lifetime as this latter is likely to suffer from unsteady combustion processes with high temporal and spatial temperature fluctuations [36] which cause matrix damage due to thermal expansion. Isotropic matrices having higher structural stiffness than foam [35], this feature can thus prevent them from suffering from the above-mentioned phenomenon.

Conclusion

This study proposed a 3D pore-resolved modeling of a single-layer porous burner based on a structured and isotropic diamond-lattice geometry. The potential of this additive printed porous medium for CPM applications has been investigated.

The macroscopic features of the CPM such as the excess enthalpy combustion and the heat recirculation through the burner have been highlighted. By studying the contribution of each heat-transfer mode involved in the recirculation process, it has been found that the lean combustion regime yields the highest

1
2
3
4 performance. It also appears that the contribution of radiation is negligible in comparison to conduction for
5 a 3D model as implemented herein.

6 A closer observation of the flow within the pores, moreover, revealed the influence of the flow regime on
7 both velocity and temperature fluctuations. Flow in nonlinear laminar regimes induces deviations that
8 increase dispersion. Although it improves both mass and heat transports, higher temperature gradients
9 occur but remain limited in comparison to the flows in open-cell foams. Lower fluctuations have finally
10 been found at low equivalence ratios and low inlet velocities, which also maximize the recirculation
11 efficiency. This supports the idea of operating porous burner in the lean-combustion regime.
12
13

14 Acknowledgements

15 The authors would like to thank Calcul Québec and Compute Canada for providing computational
16 resources.
17
18

19 Funding

20 This research did not receive any specific grant from funding agencies in the public, commercial, or not-
21 for-profit sectors.
22
23

24 Nomenclature

25 Greek symbols

Symbol	Description [SI Unit]
β	Extinction coefficient [-]
$\bar{\tau}$	Viscous stress tensor [Pa]
$\dot{\omega}$	Rate of reaction [mol/s/m ³]
Φ	Porosity [-]
δ_L	Flame thickness [m]
μ	Dynamic viscosity [kg/m/s]
ρ	Density [kg/m ³]
φ	Equivalence ratio [-]
χ	Mole fraction [-]

26 Latin symbols

Symbol	Description [SI Unit]
$D_{k,m}$	Molecular diffusivity of the specie k [m ² /s]
D_{kj}	Binary diffusion coefficient between species k and j [m ² /s]
D_L	Axial dispersion coefficient [m ² /s]
D_d^d	Thermal diffusivity due to dispersion [m ² /s]
D_p	Pore diameter [m]
h_{conv}	Heat transfer coefficient [W/m ² /K]
J	Diffusive flux [mol/m ² /s]
p	Pressure [Pa]
Pe_m	Peclet number based on molecular diffusivity [-]
Q_{ch}	Heat release [W/m ²]
\dot{q}_{cond}	Conduction heat flux [W/m ²]
\dot{q}_{conv}	Convection heat flux [W/m ²]
\dot{q}_{rad}	Radiation heat flux [W/m ²]
R	Ideal gas constant [J/mol/K]
Re_p	Pore Reynolds number [-]
T	Temperature [K]
\mathbf{u}	Velocity vector (u_x, u_y, u_z) [m/s]
	Darcy velocity [m/s]
V	Volume [m ³]
W	Molar mass [kg/mol]
Y	Mass fraction [-]

27 Abbreviations

CAD	Computer-aided design
CFD	Computational fluid dynamics
CPM	Combustion in porous media

GSR	Gas speed ratio
PPI	Pore per inch
RMS	Root mean square

Subscripts

<i>f</i>	Fluid
<i>inlet</i>	Condition at inlet boundary
<i>k</i>	Specie
<i>rms</i>	Root mean square
<i>s</i>	Solid

References

- [1] Weinberg, F.J. *Combustion Temperatures: The Future ?* Nature 1971; **233**, p. 239.
- [2] Takeno, T. and K. Sato. *An Excess Enthalpy Flame Theory*. Combustion Science and Technology 1979; **20**(1-2), p. 73-84.
- [3] Kotani, Y. and T. Takeno, *An experimental study on stability and combustion characteristics of an excess enthalpy flame*, in *Symposium (International) on Combustion*. 1982, The Combustion Institute. p. 1503-1509.
- [4] Kesting, A. and D. Trimis, *Adiabatic combustion processes in porous inert media at the lean flammability limit*, in *Proceedings of the Second International School seminar on Modern problems of combustion and its applications*. 1997: Minks (Belarus). p. 18-23.
- [5] Takeno, T., K. Sato, and K. Hase. *A theoretical study on an excess enthalpy flame*. Symposium (International) on Combustion 1981; **18**(1), p. 465-472.
- [6] Sathe, S.B., et al., *An experimental and theoretical study of porous radiant burner performance*, in *Symposium (International) on Combustion*. 1991, The Combustion Institute. p. 1011-1018.
- [7] Mathis, W.M. and J.L. Ellzey. *Flame stabilization, operating range, and emissions for a methane/air porous burner*. Combustion Science and Technology 2003; **175**(5), p. 825-839.
- [8] Mital, R., J.P. Gore, and R. Viskanta. *A study of the structure of submerged reaction zone in porous ceramic radiant burners*. Combustion and Flame 1997; **111**(3), p. 175-184.
- [9] Smucker, M.T. and J.L. Ellzey. *Computational and experimental study of a two-section porous burner*. Combustion Science and Technology 2004; **176**(8), p. 1171-1189.
- [10] Khanna, V., R. Goel, and J.L. Ellzey. *Measurements of emissions and radiation for methane combustion within a porous medium burner*. Combustion science and technology 1994; **99**(1-3), p. 133-142.
- [11] Djordjevic, N., P. Habisreuther, and N. Zarzalis. *Porous Burner for Application in Stationary Gas Turbines: An Experimental Investigation of the Flame Stability, Emissions and Temperature Boundary Condition*. Flow, Turbulence and Combustion 2012; **89**(2), p. 261-274.
- [12] Ihme, M. *NASA LEARN - Project Description*. Ihme Group [cited 2018 september 1st]; Ihme Group, Stanford Engineering; [Available from: <http://web.stanford.edu/group/ihmegroup/cgi-bin/MatthiasIhme/nasa-learn/nasa-learn-project-description/>].
- [13] Hsu, P.F., J.R. Howell, and R.D. Matthews. *A Numerical Investigation of Premixed Combustion Within Porous Inert Media*. Journal of Heat Transfer 1993; **115**(3), p. 744-750.
- [14] Dinkov, I. and H. Bockhorn, *Premixed Combustion in Porous Inert Media – Effects of the Air Equivalence Ratio and Transport Properties on the Temperature Distribution and the Peak Flame Temperature*, in *European Combustion Meeting*. 2017: Dubrovnik, Croatia.
- [15] Diamantis, D., E. Mastorakos, and D. Goussis. *Simulations of premixed combustion in porous media*. Combustion Theory and Modelling 2002; **6**(3), p. 383-411.
- [16] Mohammadi, I. and S. Hossainpour. *The effects of chemical kinetics and wall temperature on performance of porous media burners*. Heat and Mass Transfer 2013; **49**(6), p. 869-877.
- [17] Dinkov, I., P. Habisreuther, and H. Bockhorn, *Direct pore level simulation of premixed gas combustion in porous inert media using detailed chemical kinetics*, in *7th European Combustion Meeting*. 2015: Budapest (Hungary).

- 1
2
3
4 [18] Hsu, P.-F. and R.D. Matthews. *The necessity of using detailed kinetics in models for premixed combustion within porous media*. Combustion and Flame 1993; **93**(4), p. 457-466.
- 5
6 [19] Wood, S. and A.T. Harris. *Porous burners for lean-burn applications*. Progress in Energy and Combustion Science 2008; **34**(5), p. 667-684.
- 7
8 [20] Akbari, M.H., P. Riahi, and R. Roohi. *Lean flammability limits for stable performance with a porous burner*. Applied Energy 2009; **86**(12), p. 2635-2643.
- 9
10 [21] Barra, A.J., et al. *Numerical study of the effects of material properties on flame stabilization in a porous burner*. Combustion and Flame 2003; **134**(4), p. 369-379.
- 11
12 [22] Barra, A.J. and J.L. Ellzey. *Heat recirculation and heat transfer in porous burners*. Combustion and Flame 2004; **137**(1), p. 230-241.
- 13
14 [23] Hashemi, S.M. and S.A. Hashemi. *Flame stability analysis of the premixed methane-air combustion in a two-layer porous media burner by numerical simulation*. Fuel 2017; **202**, p. 56-65.
- 15
16 [24] Viskanta, R. *Modeling of combustion in porous inert media*. Special Topics & Reviews in Porous Media: An International Journal 2011; **2**(3).
- 17
18 [25] Hackert, C.L., J.L. Ellzey, and O.A. Ezekoye. *Combustion and heat transfer in model two-dimensional porous burners*. Combustion and Flame 1999; **116**(1), p. 177-191.
- 19
20 [26] Abdul Mujeebu, D.M., et al. *Trends in modeling of porous media combustion*. Progress in Energy and Combustion Science 2010; **36**(6), p. 627-650.
- 21
22 [27] Bedoya, C., et al. *Experimental study, 1D volume-averaged calculations and 3D direct pore level simulations of the flame stabilization in porous inert media at elevated pressure*. Combustion and Flame 2015; **162**(10), p. 3740-3754.
- 23
24 [28] Bedoya, C., N. Zarzalis, and P. Habisreuther. *Experimental and Theoretical Study of Combustion under Elevated Pressure within Porous Inert Media*. Energy Technology 2017; **5**(7), p. 1124-1133.
- 25
26 [29] Djordjevic, N., P. Habisreuther, and N. Zarzalis. *A numerical investigation of the flame stability in porous burners employing various ceramic sponge-like structures*. Chemical Engineering Science 2011; **66**(4), p. 682-688.
- 27
28 [30] Parthasarathy, P., P. Habisreuther, and N. Zarzalis. *Evaluation of longitudinal dispersion coefficient in open-cell foams using transient direct pore level simulation*. Chemical Engineering Science 2013; **90**, p. 242-249.
- 29
30 [31] Hayashi, T.C., I. Malico, and J.C.F. Pereira. *Three-dimensional modelling of a two-layer porous burner for household applications*. Computers & Structures 2004; **82**(17), p. 1543-1550.
- 31
32 [32] Yamamoto, K., N. Takada, and M. Misawa. *Combustion simulation with Lattice Boltzmann method in a three-dimensional porous structure*. Proceedings of the Combustion Institute 2005; **30**(1), p. 1509-1515.
- 33
34 [33] Dunnmon, J., et al. *An investigation of internal flame structure in porous media combustion via X-ray Computed Tomography*. Proceedings of the Combustion Institute 2017; **36**(3), p. 4399-4408.
- 35
36 [34] Howell, J.R., M.J. Hall, and J.L. Ellzey. *Combustion of hydrocarbon fuels within porous inert media*. Progress in Energy and Combustion Science 1996; **22**(2), p. 121-145.
- 37
38 [35] Fleck, N.A. *An overview of the mechanical properties of foams and periodic lattice materials*. Cell Met Polym 2004, p. 3-7.
- 39
40 [36] Sobhani, S., et al., *Investigation of Lean Combustion Stability, Pressure Drop, and Material Durability in Porous Media Burners*, in ASME Turbo Expo: Turbomachinery Technical Conference and Exposition. 2017: Charlotte, NC (USA).
- 41
42 [37] Durst, F. and D. Trimis. *Combustion by Free Flames Versus Combustion Reactors*. Clean Air 2002; **3**(1), p. 1-20.
- 43
44 [38] Nawada, S., S. Dimartino, and C. Fee. *Dispersion behavior of 3D-printed columns with homogeneous microstructures comprising differing element shapes*. Chemical Engineering Science 2017; **164**, p. 90-98.
- 45
46 [39] Fee, C., S. Nawada, and S. Dimartino. *3D printed porous media columns with fine control of column packing morphology*. Journal of Chromatography A 2014; **1333**, p. 18-24.
- 47
48 [40] Sobhani, S., et al. *Modulation of heat transfer for extended flame stabilization in porous media burners via topology gradation*. Proceedings of the Combustion Institute 2019; **37**(4), p. 5697-5704.
- 49
50
51
52
53
54
55
56
57
58
59
60
61
62
63
64
65

- 1
2
3
4 [41] Sobhani, S., et al., *Enabling Tailored Porous Media Burners via Additive Manufacturing*, in *11th U.S. National Combustion Meeting*. 2019: Pasadena, CA, USA.
- 5
6 [42] Samoilenko, M., et al. *Design, manufacture and testing of porous materials with ordered and random porosity: Application to porous medium burners*. Applied Thermal Engineering 2019; **158**, p. 113724.
- 7
8
9 [43] Ahmadi, S.M., et al. *Mechanical behavior of regular open-cell porous biomaterials made of diamond lattice unit cells*. Journal of the Mechanical Behavior of Biomedical Materials 2014; **34**, p. 106-115.
- 10
11 [44] Rajani, B.N., A. Kandasamy, and S. Majumdar. *Numerical simulation of laminar flow past a circular cylinder*. Applied Mathematical Modelling 2009; **33**(3), p. 1228-1247.
- 12
13 [45] Zhang, J. and C. Dalton. *A three - dimensional simulation of a steady approach flow past a circular cylinder at low Reynolds number*. International Journal for Numerical Methods in Fluids 1998; **26**(9), p. 1003-1022.
- 14
15 [46] Liu, H., et al. *Parametric investigations of premixed methane-air combustion in two-section porous media by numerical simulation*. Fuel 2010; **89**(7), p. 1736-1742.
- 16
17 [47] CD-Adapco, *STAR-CCM+ Documentation*. 2016.
- 18 [48] EngiCer, *Material Data Sheet: SiSiC*.
- 19 [49] Westbrook, C.K. and F.L. Dryer. *Simplified Reaction Mechanisms for the Oxidation of Hydrocarbon Fuels in Flames*. Combustion Science and Technology 1981; **27**(1-2), p. 31-43.
- 20 [50] Kundu, P., V. Kumar, and I.M. Mishra. *Experimental and numerical investigation of fluid flow hydrodynamics in porous media: Characterization of pre-Darcy, Darcy and non-Darcy flow regimes*. Powder Technology 2016; **303**, p. 278-291.
- 21 [51] Ergun, S. *Fluid Flow through Packed Columns*. Chemical Engineering Progress 1952; **48**(2), p. 89-94.
- 22 [52] Fand, R.M., et al. *Resistance to the Flow of Fluids Through Simple and Complex Porous Media Whose Matrices Are Composed of Randomly Packed Spheres*. Journal of Fluids Engineering 1987; **109**(3), p. 268-273.
- 23 [53] Turns, S.R. *An introduction to combustion : concepts and applications*, ed. 3. 2012, New-York, NY: McGraw-Hill.
- 24 [54] Smith, G.P., et al. *GRI-Mech 3.0*. 2000 // 1 juin 2018]; Available from: http://www.me.berkeley.edu/gri_mech/.
- 25 [55] Poinso, T. and D. Veynante. *Theoretical and numerical combustion*, ed. 2. 2005, Philadelphia, PA: RT Edwards, Inc.
- 26 [56] Djordjevic, N., *Flammenstabilisierung durch Verbrennung in festen Schwämmen*. 2011, Karlsruhe Institute of Technology: Karlsruhe, Germany.
- 27 [57] Talukdar, P., et al. *Heat transfer characteristics of a porous radiant burner under the influence of a 2-D radiation field*. Journal of Quantitative Spectroscopy and Radiative Transfer 2004; **84**(4), p. 527-537.
- 28 [58] Hashemi, S.M. and S.A. Hashemi. *Investigation of the premixed methane-air combustion through the combined porous-free flame burner by numerical simulation*. Proceedings of the Institution of Mechanical Engineers, Part A: Journal of Power and Energy 2019, p. 773-785.
- 29 [59] Coutinho, J.E.A. and M.J.S. de Lemos. *Laminar flow with combustion in inert porous media*. International Communications in Heat and Mass Transfer 2012; **39**(7), p. 896-903.
- 30 [60] Pereira, J.M.C., et al. *Quasi-1D and 3D TPOX porous media diffuser reformer model*. Fuel 2010; **89**(8), p. 1928-1935.
- 31 [61] Bear, J. *Dynamics of fluids in porous media*. 2013, New-York, NY: Dover Publication.
- 32 [62] Prausnitz, J. *Longitudinal dispersion in a packed bed*. AIChE Journal 1958; **4**(1), p. 14M-22M.
- 33 [63] Taylor, G. *Dispersion of soluble matter in solvent flowing slowly through a tube*. Proc. R. Soc. Lond. A 1953; **219**(1137), p. 186-203.
- 34 [64] Delgado, J.M.P.Q. *Longitudinal and Transverse Dispersion in Porous Media*. Chemical Engineering Research and Design 2007; **85**(9), p. 1245-1252.
- 35
36
37
38
39
40
41
42
43
44
45
46
47
48
49
50
51
52
53
54
55
56
57
58
59
60
61
62
63
64
65